Constructing Pd/ferroelectric $Bi_4Ti_3O_{12}$ nanoflake interfaces for O_2 activation and boosting NO photo-oxidation

Qian Zhang [a,b], Yuanyu Shi [d], Xianjin Shi [a,c], Tingting Huang [a], Shuncheng Lee [e], Yu Huang [a,b,*], Jun-ji Cao [a,b,*]

[a] State Key Laboratory of Loess and Quaternary Geology (SKLLQG), Key Laboratory of Aerosol Chemistry and Physics, Institute of Earth Environment, Chinese Academy of Sciences (CAS), Xi'an, 710061, China
[b] CAS Center for Excellence in Quaternary Science and Global Change, Xi'an, 710061, China
[c] University of Chinese Academy of Sciences, Beijing, 100049, China
[d] Hohai University, Nanjing, 211100, China
[e] Department of Civil and Environmental Engineering, The Hong Kong Polytechnic University, Hong Kong, China

ARTICLE INFO

ABSTRACT

Photo-oxidative NO_x removal often encountered with sluggish charge carrier separation kinetics and poor selectivity. Herein, Pd/ferroelectric $Bi_4Ti_3O_{12}$ nanoflakes (Pd/BTO NF) were constructed to investigate the photo-excited charge separation, O_2 activation and the generated reactive oxygen species (ROS) in dictating NO removal. Results showed that the depolarization field of ferroelectric BTO NF significantly promoted bulk charge separation, leading to boosted NO removal reaction kinetics (10 times higher) for Pd/BTO NF comparing with Pd/TiO$_2$. Revealed by electronic paramagnetic resonance and radical scavenging tests, it is observed that the primary O_2 activation species differed among Pd, Ag and Pt supported BTO NF photocatalysts, which resulted in different selectivity. The underlying mechanism of NO photo-oxidative conversion pathway was studied by *in situ* diffuse reflectance infrared Fourier transform spectroscopy. This work illustrate that metal/ferroelectric interfaces can be tuned to obtain differing O_2 activation species, and notable selectivity changes in photocatalysis mediated environmental remediation reactions.

1. Introduction

Nitrogen oxides (NO_x) are important precursors of $PM_{2.5}$, and they are involved in ozone pollution, both of which have substantially increased the global burden of disease over the past 25 years, as these pollutants can cause heart, pulmonary, and respiratory disease [1–3]. At present, the selective catalytic reduction with NH_3 and three-way catalysis are the most mature technologies for reducing NO_x emissions from primary sources such as coal-fired power plants and gasoline vehicles [4,5]. However, these methods are energy-intensive involving high temperatures ($> 200\ °C$), and large quantities of NO_x (as high as 1000–2000 ppm) can be discharged into atmosphere due to catalyst deactivation or inevitable releases [6]. Therefore, an economic and environmental-friendly way for NO_x remediation is urgently needed and worth pursuing. Recently, a notable study showed that direct capture of NO_2 and conversion into HNO_3 was achieved under ambient conditions

using metal-organic framework nanomaterials [6]. That approach provides a potential route for simultaneous waste recycling and the production of important feedstock for fertilizer.

Photocatalytic conversion of NO_x into nitrates has aroused considerable attention in recent years, because of the effectiveness for purification and involving mild conditions. Nitrogen dioxide, which is the main intermediate in the photocatalytic oxidation process, is 8–25 times more dangerous than NO and leads to secondary pollution [7]. To enhance nitrate selectivity, several strategies have been proposed, including element doping, Fe(III) ion grafting, hydrophobic TiO_2/HZSM-5 zeolite composite construction, and Z-scheme heterojunction construction (perylene imides-*g*-C_3N_4) [7–10]. Apart from those strategies, enhancing O_2 activation has been recently put forward to improve nitrate selectivity. For example, Folli et al. synthesized $Ti_{0.909}W_{0.091}O_2N_x$ nanoparticles and demonstrated that reduced tungsten centers could enable multi-electron transfer for molecular oxygen

reduction, thus enhancing the selectivity for nitrate [11]. Shang et al. proposed that defect engineered-BiOCl and blue TiO_2 bearing oxygen vacancies favored O_2 activation and the generation of superoxide radicals ($\bullet O_2^-$), thereby converting NO directly to nitrates and simultaneously suppressing NO_2 formation [12,13].

Platinum group metals often have been applied as co-catalysts during photocatalysis owing to their excellent O_2 adsorption-activation and charge separation abilities [14,15]. In recent studies, Fujiwara et al. reported Pd subnano-clusters and single atom anchored TiO_2 showed superior selectivity for NO photo-oxidation towards nitrate formation [16,17]. The high conversion rate and selectivity were mainly ascribed to the strong metal-support interactions (SMSI) *via* oxygen defects on TiO_2 surfaces, which can maintain the state of isolated Pd atoms and prevent nitrate poisoning. The role of O_2 activation in NO photo-oxidation, however, was not explained. The mechanisms for O_2 activation can vary dramatically, depending on the type of deposited metals, particle sizes, and exposed facets of support as well as electronic interactions within the metal-support interface [18]. Through a combination of electronic paramagnetic resonance spectroscopy and finite-temperature *ab initio* simulations, Siemer et al. concluded that gold/titania interface perimeters were active sites for adsorbed O_2 reduction by photo-excited electrons that migrated from TiO_2 [19]. Huang et al. reported that defect-free Au/TiO_2 interfaces favored O_2 activation more than oxygen vacancy (V_o) rich Au/TiO_2 interfaces because V_o can trap photo-excited electrons, thus preventing interactions with O_2 [20]. For the aerobic oxidation of 2-PrOH under visible light, $Pt-Ta_2O_5$ exhibited the best activity among several supports, including TiO_2, CeO_2, ZrO_2 and $SrTiO_3$. This was attributed to strong Pt/Ta_2O_5 interactions, which increased the electron density of Pt particles and activated O_2 directly under illumination to produce peroxide species for oxidation [21]. Likewise, the results of a theoretical study by Brugnoli et al. showed that Ag_{10}/CeO_2 exhibited higher O_2 adsorption and greater dissociation ability than Ag_{10}/TiO_2 due to the superior electron storage and release of ceria [22]. Applying these strategies to NO removal, the choice of deposited metal types, supports, and their interfaces may result in unique charge kinetics and O_2 activation mechanisms.

$Bi_4Ti_3O_{12}$ is an Aurivillius-type layered perovskite oxide with ferroelectric properties. It has a high Curie temperature of 675 °C, which implies that it maintains a stable ferroelectric phase at room temperature [23]. The crystal structure is stacked with $[Bi_2O_2]^{2+}$ layers and interleaved $[TiO_6]$ octahedra, and the distortion of $[TiO_6]$ octahedra is usually the cause of ferroelectric spontaneous polarization. Liu et al. demonstrated that in single-domain ferroelectric $PbTiO_3$ nanoplates, the internal unscreened depolarization field is the main driving force for photo-excited charge separation [24]. More importantly, the unscreened depolarization field intensity is far greater than that of space charge regions, and it can be maintained throughout the entire particle [24]. Very recently, it is reported that using corona discharge to enhance ferroelectric polarization has drawn increasing interest [25,26]. Therefore, adopting ferroelectric nanomaterials for use as photocatalysts is one of the most promising strategies for optimizing the photogenerated charge-separation process. To understand the process, it is important to determine how the photogenerated electrons are distributed and transferred across the metal/ferroelectric support interface and how this in turn affects O_2 activation mechanism and photocatalytic NO removal. To the best of our knowledge, this has not been investigated and reported so far.

Herein, we describe the preparation of Pd nanoparticles-supported ferroelectric $Bi_4Ti_3O_{12}$ nanoflakes (hereinafter denoted as Pd/BTO NF) photocatalyst, using a fast and energy-efficient microwave synthesis method and a photo-deposition strategy. Microwave synthesis has become a green and popular approach for preparing a diversity of nanostructures in recent decades [27]. The effect of supports, metal types, and the interface between Pd and $Bi_4Ti_3O_{12}$ on reactive oxygen species (ROS) generation and NO photooxidation performance were

examined. Piezoelectric force microscopy (PFM), photoluminescence spectroscopy (PL), electron paramagnetic resonance (EPR) analyses, temperature-programmed oxygen desorption (O_2-TPD) and density functional theory (DFT) simulations were employed to characterize the charge separation and O_2 activation behavior. Reaction mechanisms were explored by using *in situ* infrared spectroscopy. The objective of this study was to construct and tune novel metal/ferroelectric oxide interfaces for visible light absorption, charge separation and O_2 activation, and to optimize the material for environmental remediation applications. This study provides a reliable synthetic strategy for perovskite nanomaterials, and introduces the effect of ferroelectric depolarization field to enhance photocatalytic performances.

2. Experimental

2.1. Synthesis of Pd/Bi₄Ti₃O₁₂ nanoflakes

All chemicals used for the synthesis were of analytical grade and used as received without further purification. For the precursor preparation, Milli-Q water (18.2 MΩ) produced from the UltraPure® water purification system (Millipak200) was used.

For the synthesis of $Bi_4Ti_3O_{12}$ nanoflakes, stoichiometric amounts of $Bi(NO_3)_3.5 H_2O$ and amorphous TiO_2 were dissolved in a mixture of H_2O (4.5 mL) and nitric acid (1.5 mL) for 40 min under vigorous stirring. NaOH (3 M) was added dropwise to the mixture which was continuously stirred for another 30 min. The precursor was then transferred to a Teflon® reaction vessel (50 mL) and subjected to microwave irradiation (Multiwave PRO, Anton Parr, Austria). The reaction vessel was heated with a temperature ramp at 800 W to 200 °C (infrared sensor detection) and maintained at that temperature for 60 min. After the procedure was finished, the product was separated by centrifugation, washed thoroughly with ultrapure water to neutral pH and dried overnight at 80 °C. The dried product, denoted as BTO NF, was calcined at 400 °C in air for 2 h.

For the preparation of $Pd/Bi_4Ti_3O_{12}$ nanoflakes (Pd/BTO NF), Pd nanoparticles were photo-deposited onto the BTO NF surface. Before the UV light treatment, as described below, an aqueous solution of the as-prepared BTO NF (0.2 g) and Na_2PdCl_4 (5 mg mL^{-1}) was mixed in 10 mL ultrapure water, to give a loading amount of 0.5 wt%. For the UV treatment, the dispersion was stirred for 30 min, followed by a thorough water rinse and centrifugal separation and finally dried in vacuum. Illumination was provided by a Xenon-lamp (Perfectlight, PLS-SXE300UV, Beijing) equipped with a 365 nm band pass filter. The power density of the UV light at an operating current of 20 A was measured to be 128 mW cm^{-2} by a radiometer (Thorlabs, PM100D, the United States). For comparison, Ag/BTO NF and Pt/BTO NF with the same loading amount were also prepared by the photo-deposition procedure. Pd/TiO_2 was also prepared by replacing BTO NF with commercial anatase TiO_2 (Aladdin, Shanghai).

2.2. Photocatalyst characterization

The X-ray diffraction (XRD) patterns of photocatalyst powders were obtained with the use of a PANalytical X'pert Pro diffractometer (PANalytical Corp., the Netherlands), which had a scanning rate of 0.017° min^{-1} and covered a range from 20° to 80°. Scanning electron microscope (SEM) images were obtained on a Tescan microscope (Tescan Corp., MAIA3, Czech). For transmission electron microscopy (TEM), high-resolution TEM (HR-TEM) and selected area electron diffraction (SAED) characterization, images were taken on the JEOL 2010 instrument at accelerating voltage of 200 kV (JEOL Corp., Japan). The atomic high-angle annular dark-field (HAADF) scanning transmission electron microscopy (STEM) and energy dispersive X-ray spectrometry (STEM-EDS) mapping observations, were collected on a JEM 3010 electron microscope (JEOL Corp., Japan) that operated at 200 kV. The loaded Pd content was characterized by an Agilent 725 ICP-OES instrument

(Agilent, the United States). Atomic force microscope (AFM) images were obtained using a Multimode 8 instrument (Bruker, Germany) equipped with a MESP-RC probe that had Co/Cr coated tips (resonant frequency 72 kHz). Piezoelectric force microscope (PFM) measurement was conducted using the same Multimode 8 instrument instrument with a SCM-PIT-V2 probe with Pt/Ir coating cantilever. X-ray photoelectron spectroscopy (XPS) was performed using an Escalab 250Xi photoelectron spectrometer (ThermoFisher Scientific, the United States), with sample irradiation by a monochromatic Al Kα X-ray source ($h\nu$ = 1486.71 eV). All binding energies were calibrated by C 1 s at 284.6 eV as a reference, and for the background subtraction the Shirley method was used. Ultraviolet-Visible diffuse reflectance spectra (UV–vis DRS) were collected using an Agilent Cary 100 spectrophotometer (Agilent Corp., the United States) equipped with an integrating sphere, and using $BaSO_4$ reflection as a reference. Sample bandgaps were calculated by converting the reflection into absorbance through Kubelka-Munk function. The specific surface areas of the samples were determined by N_2 adsorption-desorption isotherms at 77 K (Micrometrics, ASAP 2020, the United States), using the Brunauer-Emmett-Teller (BET) method. The photoluminescence (PL) spectra of samples were collected on the Fluoromax-4 spectrophotometer (Horiba Scientific, France) with excitation at λ = 325 nm. The transient photocurrent measurement was performed on a Parstat 4000 potentiostat (Princeton, the United States) using the three-electrode configuration in a single cell with quartz window. The Ag/AgCl/KCl electrode and Pt foil were served as reference and counter electrodes, respectively. The working electrode (photoanode) was prepared by dip-coating BTO NF/1 wt% Nafion/ethanol suspension on FTO glass and tested in 0.1 M Na_2SO_3 electrolyte under monochromatic LED light of 405 nm wavelength. Mott-Schottky (M-S) plots of BTO NF were also obtained on the same potentiostat. Detailed testing parameters can be found in Supporting Information.

2.3. Photocatalytic NO oxidation under visible light

A glass petri dish (80 mm in diameter) coated with 0.1 g photocatalyst was placed in a continuous-flow stainless steel chamber (4.5 L) with quartz window on top and irradiated with visible light from a Xe lamp with an UV-cutoff filter (λ > 420 nm). The optical power density output was measured to be 2.14 W cm^{-2} (Thorlabs, PM100D, the United States). Before irradiation, an air stream containing 400 ppb of NO (balanced by zero air) from a gas dilution calibrator (Sabio 4010, the United States) was feed into the chamber at flow rate of 1 L min^{-1}. The concentrations of NO, NO_2 and NO_x were continuously monitored by a chemiluminescence NO_x detector (Ecotech EC9841, Australia) at the chamber outlet. The measurements were conducted at room temperature and a relative humidity of 40 ± 5%. After allowing the reactions to proceed for 40 min, NO removal (η_{NOx}) and NO_2 generation (σ_{NO2}) were calculated as follows:

$$\eta_{NO} (\%) = (1 - C_{NO\text{-}out}) / C_{NO\text{-}in}$$

$$\sigma_{NO2} = C_{NO2\text{-}out} - C_{NO\text{-}in}$$

The NO removal rate constants were calculated assuming first-order reaction kinetics and plotting $ln (C/C_0)$ against reaction time *t*.

2.4. Mechanistic studies

Scavenging tests were performed using the same procedure as for the photocatalytic NO oxidation tests, but with scavengers (isopropanol, benzoquinone, potassium dichromate and potassium iodide) included to capture selected active species.

Electron paramagnetic resonance (EPR) spectra were recorded at the X-band (9.8 GHz) using a Bruker continuous wave (cw)-EPR instrument (ELEXSYS-II E500, Germany) with 100 kHz magnetic field modulation at a microwave power of 22.0 mW. Photocatalyst samples were placed in a quartz EPR tube mixed with 5,5-dimethyl-L-pyrroline N-oxide (DMPO,

100 mM) as the spin-trapping agent. A 300 W Xe lamp (Perfectlight, Beijing) with a 420-nm cutoff filter was used as the light source.

Temperature-programmed desorption of O_2 (O_2-TPD) and NO (NO-TPD) experiments were conducted using a chemisorption analyzer (BJbuilder, PCA 1200, Beijing), with powder samples (100 mg) supported on a frit in a continuous flow quartz reactor. Before O_2 adsorption, the samples were pretreated under He flow at 100 °C for 30 min at heating rate of 10 °C min^{-1}. After cooling to room temperature, the samples were subjected to O_2 flow (100 ppm) for 40 min at room temperature. Once equilibrated, the pretreated samples were heated to 800 °C at a ramping rate of 8 °C min^{-1} under He flow (30 mL min^{-1}). The desorbed species were monitored using a thermal conductor detector. For the NO-TPD tests, O_2 adsorption was replaced with NO, while keeping other experimental parameters unchanged.

In situ diffuse reflectance infrared Fourier transform spectroscopy (DRIFTS) measurements were made with the use of a Nicolet iS50FT-IR spectrometer (Thermo, USA), equipped with an *in situ* diffuse reflectance cell. A photocatalyst (20 mg) was placed in the DR cell and heated under He flow to 100 °C for 30 min and then cooled to room temperature. The IR spectrum of each pretreated catalyst was recorded and taken as the background reference and later subtracted from the appropriate spectrum. The DR cell was purged with a mixture of NO + O_2 (25 mL min^{-1} and 5 mL min^{-1}, respectively) for adsorption in the dark. After 30 min, the samples were photo-irradiated with the use of a Xe lamp (300 W, Perfectlight, Beijing) equipped with a 420 nm cutoff filter. The IR spectra were collected during dark and light periods in time sequence through a mercury-cadmium-telluride detector.

2.5. Computational details

The density functional theory (DFT) calculations were performed with Vienna Ab Initio Simulation Package (VASP) [28,29], using a plane-wave cutoff energy of 400 eV, and the projector augmented wave pseudopotentials to describe the inner-shell electrons. Spin-polarized calculations were employed using the generalized gradient approximation (GGA) with the Perdew-Burke-Ernzerhof (PBE) to describe the exchange-correlation energy and electron interactions. For the structure geometry optimization, Brillouin zone was sampled by 2 × 2 × 1 *k*-points using the Monkhorst-Pack scheme to relax the super cell [30]. The geometries were not optimized until the energy differences between two electronic optimization steps converge to 1.0×10^{-5} eV/atom, and the force is less than 2×10^{-2} eV/Å, respectively. The calculated charge density difference and Bader charge analysis was conducted to describe the electrons transfer.

3. Results and discussion

3.1. Preparation, morphology and structural analysis of Pd/Bi$_4$Ti$_3$O$_{12}$ nanoflakes

The Pd/BTO NF samples were prepared by a microwave irradiation procedure followed by photo-deposition (Fig. S1). An optimized microwave output power (800 W) and reaction time (60 min) recipe was developed to ensure the complete collection of BTO NF products. The XRD pattern showed that pure crystalline orthorhombic-structured $Bi_4Ti_3O_{12}$ with primary diffraction peaks were matched with the standard PDF file (JCPDS No. 72-1019), space group *Aba2*(41), suggesting the successful synthesis through the microwave approach [31]. By contrast, poorly developed diffraction peaks were found for hydrothermally-derived BTO in a 12-hr reaction (Fig. 1a). This suggests that the rapid heating associated with microwave irradiation accelerates the nucleation and growth of perovskite nanostructures, and this demonstrates the potential advantages of updating the conventional, time-consuming, solid-state or hydrothermal synthetic processes [32]. The deposition of Pd nanoparticles did not introduce diffraction peaks of Pd or PdO$_x$ phase, but decreased primary diffraction peak intensity of
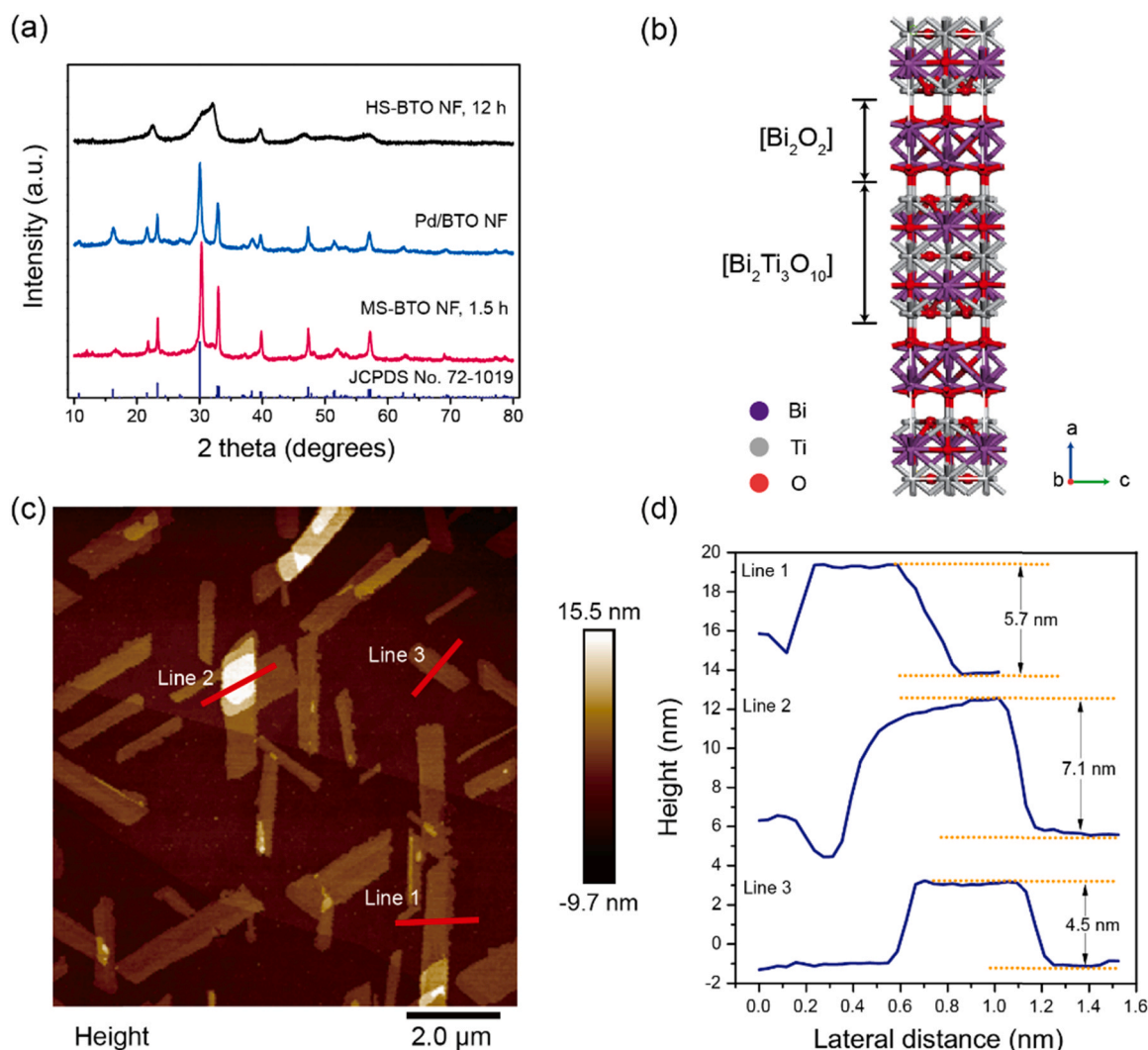
Fig. 1. (a) X-ray diffraction patterns of the hydrothermally synthesized $Bi_4Ti_3O_{12}$ ferroelectric nanoflakes (HS-BTO NF), microwave synthesized BTO NF (MS-BTO NF), and Pd/BTO NF. (b) The simulated crystal structure models of BTO as viewed along the [010] direction. (c, d) Atomic force microscopy image and the corresponding height (or thickness) profiles of the synthesized BTO NF.

BTO NF was observed, implying a small size and good dispersion of Pd during the photo-deposition process. As shown in Fig. 1b, the crystal structure of BTO NF is composed of alternating $[Bi_2O_2]^{2-}$ and $[Bi_2Ti_3O_{10}]^{2+}$ layers, where the TiO_6 octahedra is regularly located in the structure and Bi atoms are inserted into the space. The AFM images (Fig. 1c and d) showed that the BTO exhibited a 2D flake-like structure with smooth surfaces, and the average nanoflake thickness was in the range of 3–6 nm.

The morphology and microstructure of the as-prepared samples were characterized by a series of electron microscopy techniques. Field-emission scanning electron microscopy (FE-SEM) images show Pd/BTO nanoflakes mainly consist of sheet-like morphology with lateral size of ~ 400–600 nm and thickness of ~ 30 nm (Fig. 2a). Under the high voltage circumstances, very thin nanoflakes would become transparent and undetectable, which may explain the difference in thickness as compared with the AFM result. The morphology is similar to that reported for $Bi_4Ti_3O_{12}$ nanosheets prepared by a conventional sol-gel hydrothermal process [31]. The TEM images in Fig. 2b and c showed that Pd nanoparticles (14 ± 2 nm in diameter) were randomly distributed on the crystalline BTO NF, and the lattice fringe of 0.23 nm and 0.27 nm interplanar spacing corresponded to the Pd (111) plane and BTO (100) plane, respectively. The SEM and TEM images of pristine BTO NF can be found in Figs. S2(a–d) for references. The content of Pd loaded

on BTO NF was determined by inductively coupled plasma optical emission spectrometry (ICP-OES) analysis to be 0.44 wt%, which is close to the nominal value.

To get further insight into the crystal structure, we conducted atomic imaging of Pd/BTO NF using an aberration corrected scanning transmission electron microscopy (AC-STEM). Fig. 2d shows an HAADF-STEM image of Pd/BTO nanoflake with highly-ordered arrangement of atoms, where the O atoms are invisible in the high-angle annular dark-field mode. The arrangement of Bi and Ti atoms from the top view can be perfectly matched with the (100) crystallographic plane of BTO crystal model. The lattice fringes of 0.273 and 0.272 nm (marked by yellow solid line) are indexed to (0012) and (020) crystallographic plane of BTO, respectively, and they are perpendicular to each other. However, no Pd single atoms or clusters were observed, probably due to the low contrast and excellent dispersion over the BTO lattice [33]. The STEM-EDS elemental mapping in Fig. 2e reveals the homogeneous distribution of Bi, Ti, O and Pd elements, and the atomic ratio of Bi/Ti is about 2.5, nearly twice higher than the stoichiometric ratio. This indicates that the synthesized $Bi_4Ti_3O_{12}$ is bismuth rich on surface and can explain the color appearance of pale yellow.

X-ray photoelectron spectroscopy was used to investigate the electronic state of Pd species and electronic interactions between Pd and the BTO NF support. The XPS peaks appearing at 159.2 and 164.5 eV with
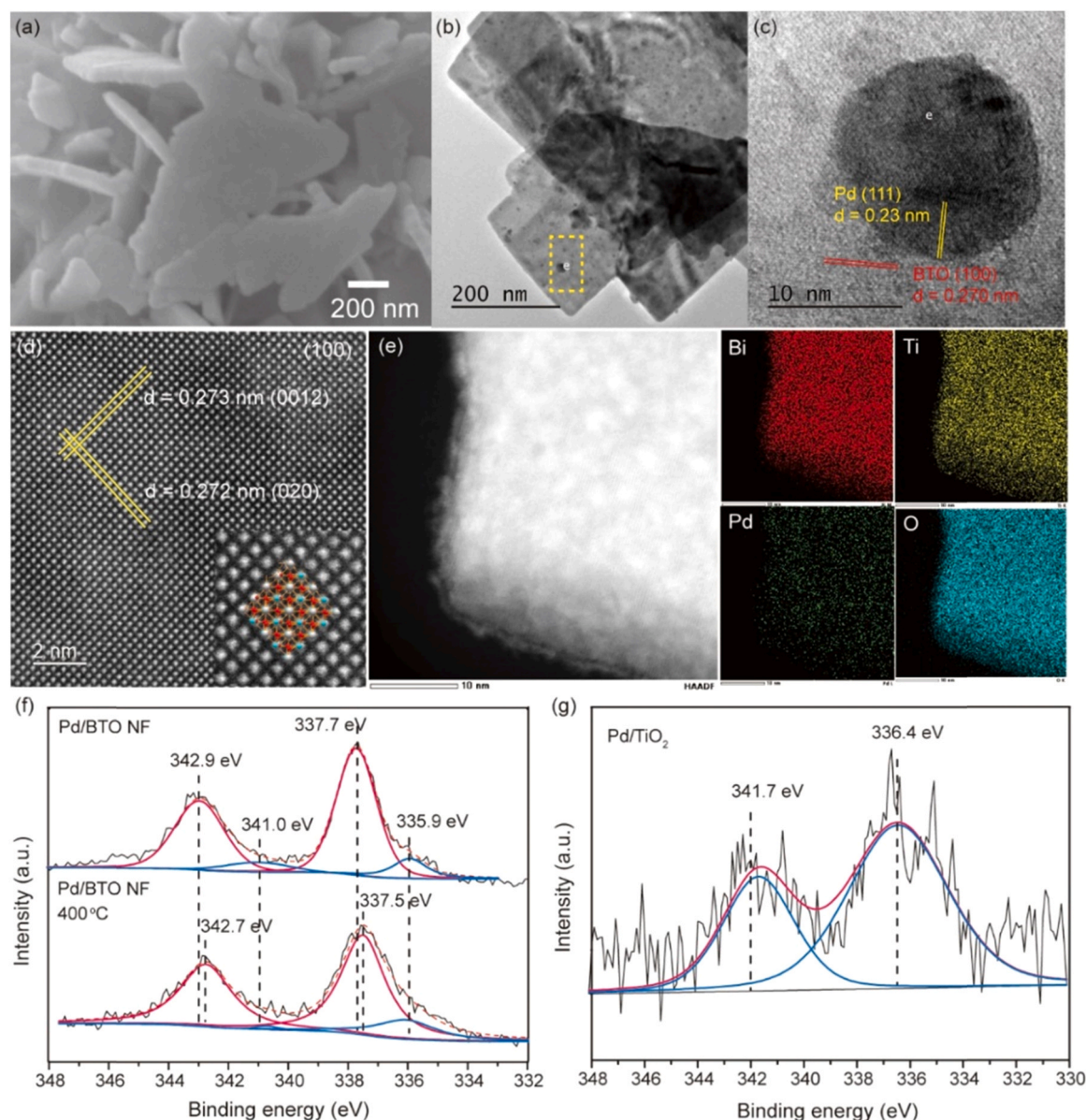
Fig. 2. (a) Field-emission scanning electron microscopy (FE-SEM) image of Pd/BTO NF. (b and c) Transmission electron microscopy (TEM) and high-resolution TEM images of Pd/BTO NF showing a good dispersion of Pd nanoparticles on the BTO NF support. (d) High-angle annular dark-field scanning transmission electron microscopy (HAADF-STEM) image of typical BFO NF and corresponding crystal structure from the top view. (e) Energy-dispersive X-ray spectroscopic elemental mapping of the selected area. (f and g) High resolution XPS of Pd $3d$ orbital of Pd/BTO NF before and after calcination at 400 °C in air, compared with Pd $3d$ orbital of Pd/TiO$_2$.

splitting binding energy of 5.3 eV demonstrated the existence of Bi^{3+} state in the BTO NF (Fig. S3a), and the peaks observed at 458.0 and 463.5 eV with splitting energy of 5.5 eV also proved the existence of Ti^{4+} in the BTO NF (Fig. S3b). To characterize the electronic state of Pd species, Fig. 2f shows that the Pd $3d_{5/2}$ orbital peaks were broad and could be split into a dominant peak at binding energy ∼ 337.7 eV and a small peak at 335.9 eV. This suggests that the Pd surface was predominantly composed of Pd^{4+} state on the BTO NF support [16,33]. Calcination at 400 °C evidently did not induce any remarkable changes in the Pd electronic state, suggesting that strong metal-support interaction existed across the interface. Compared with Pd/BTO NF, the Pd species in the Pd/TiO$_2$ was characteristic of Pd^{2+} state because of the Pd $3d_{5/2}$ binding energy located at 336.4 eV (Fig. 2g). The large chemical shift in Pd/BTO NF relative to metallic Pd state and the stability during calcination could be ascribed to the strong metal-support interactions [34]. This suggests that different states of Pd and the interaction with support

could be achieved by changing TiO$_2$ with ferroelectric BTO NF. For Ag/BTO NF and Pt/BTO NF, the Ag state was found to be metallic Ag with Ag $3d_{5/2}$ orbital binding energy at 367.4 eV, whereas the Pt state was observed to keep the oxidized Pt^{2+} state with Pt $4f_{7/2}$ orbital binding energy at 73.04 eV (Fig. S3c) [35,36]. This could be attributed to the weak metal-support interactions between Ag and the BTO NF support.

3.2. Photocatalytic performance for NO removal

The photocatalytic performance of Pd/BTO NF for NO oxidation was evaluated and compared with different types of metals and oxide supports. The experiments were conducted in a stainless-steel reactor with quartz window and a Xe lamp for irradiation ($\lambda > 420$ nm). All photocatalysts are inactive for NO removal without light irradiation. We initially examined the effect of the Pd loading amount on the photocatalytic performance for 40 min and found that the Pd/BTO NF

displayed Pd loading amount-dependent activity (Fig. S4a). Of the photocatalysts tested, 0.5 wt% Pd/BTO NF exhibited the best performance and further Pd loading was found to be disadvantageous. This could be tentatively explained as that the Pd species enhanced visible light absorption (Fig. S4b), but higher loading amount would promote particle growth and suppress effective charge injection. Therefore, we conducted the following experiments using 0.5 wt% Pd/BTO NF and made comparisons with Pt or Ag nanoparticles supported on BTO NF.

As shown in Fig. 3a, the Pd/BTO NF displayed the best performance

(a)

(b)

(c)
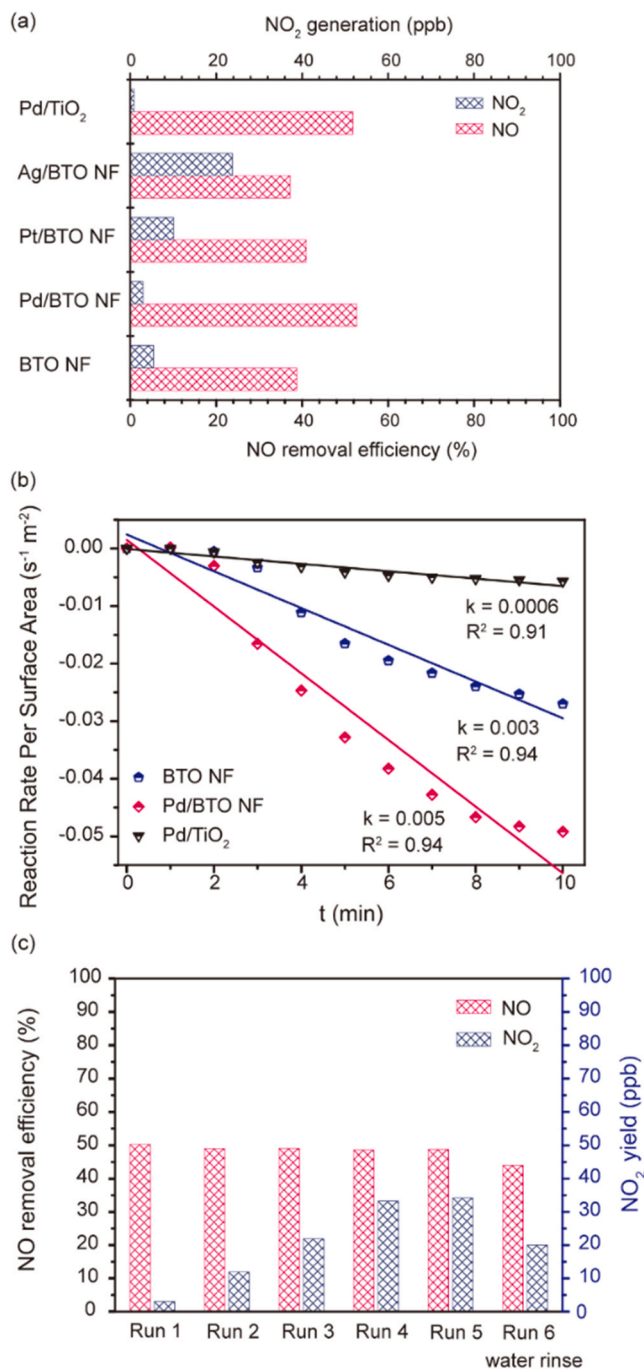
Fig. 3. Photocatalytic performances. (a) NO removal efficiencies and NO_2 formation over various photocatalysts for 40 min (b) Comparison of the NO removal rates over BTO NF, Pd/BTO NF and Pd/TiO$_2$ photocatalysts. (c) Stability performance of Pd/BTO NF for NO photooxidation during 4 h. Reaction conditions: 400 ppb NO balanced with zero air at flow rate of 1 L min^{-1}; 300 W Xe lamp equipped with UV cut-off filter ($\lambda > 420$ nm).

for NO removal with $\eta > 50\%$ and minor σ_{NO2} for a 40 min reaction under visible light. Compared with Pd/BTO NF, BTO NF loaded with Pt or Ag nanoparticles exhibited little or no activity enhancement. In addition, the highest yield of NO_2 was generated over Ag/BTO NF, resulting in low selectivity for NO_3^- formation. Although Pd/TiO$_2$ exhibited performance similar to that Pd/BTO NF for NO removal, it should be noted that the commercial anatase TiO$_2$ we employed had a large surface area of 113.96 m^2 g^{-1}, whereas the as-prepared BTO NF only possessed a smaller surface area of 11.96 m^2 g^{-1}. To make comparisons, the reaction rate per unit surface area as a function of irradiation time was plotted for BTO NF, Pd loaded TiO$_2$ and BTO NF (Fig. 3b). An extraordinarily high reaction rate of 5×10^{-3} s^{-1} was obtained for Pd/BTO NF, almost 8.4 times as that for Pd/TiO$_2$. To sum up, it is worth noting that Pd/BTO NF, Ag/BTO NF, Pt/BTO NF and Pd/TiO$_2$ exhibit remarkably distinct activity and selectivity toward NO_3^- production, indicating that both metal nanoparticles and support play crucial roles in O$_2$ activation process and detailed characterizations are needed to clarify the differences.

To promote Pd nanoparticles adhere firmly on the BTO NF support, we annealed the Pd/BTO NF sample at 400 °C for 1 h in air. However, the annealed photocatalyst showed decreased activity for NO$_x$ removal (Fig. S4c), probably due to the sintering of Pd nanoparticles into larger particles at high temperature that leads to poor charge injection [21]. Finally, the stability of Pd/BTO NF was examined by exposing the photocatalyst to five repeated runs for a total irradiation of 4 h. As shown in Fig. 3c, the photocatalyst maintained relatively stable performance for NO removal, whereas the NO_2 production increased gradually after the first run. After the sample was rinsed with deionized water and subjected to a sixth run, the NO_2 yield decreased remarkably. Therefore, we mainly ascribed the progressive deteriorative selectivity under prolonged light irradiation to a result of the reaction $NO_3^- + NO \rightarrow 2NO_2$.

3.3. The origin of activity enhancement

3.3.1. Optical and charge separation properties

Since the light harvest properties of deposited noble metal nanoparticles strongly affect the photo-excited charge carrier utilization and photocatalytic performance, the UV–vis diffuse reflectance spectroscopy was carried out. Different from the previous literature results that BTO mainly exhibited optical response at wavelengths < 450 nm, the as-prepared BTO NF in this work extend the absorption range into visible light with wavelengths at 500 nm (Fig. 4a), which is equivalent to a band gap of 2.75 eV [31,37]. This is probably related with the bismuth rich character of BTO NF that leads to hybridization of Bi *6s* with O *2p* orbitals and thereby narrowed band gap. Compared with the pristine BTO NF, the deposited Ag/BTO NF exhibited the surface plasma resonance (SPR) enhanced absorption peak around 550 nm due to Ag nanoparticles; [35] the Pd/BTO NF also exhibited a broad absorption band across the visible light region, which we ascribe to the interband transition of *d-d* orbital electrons on Pd nanoparticles. The Pt/BTO NF showed weak absorption enhancement in the visible light region. This partially explains the activity enhancement, but other factors may also be involved to trigger selectivity differences.

The ferroelectric spontaneous polarization greatly affects the photo-excited charge carrier separation of ferroelectric semiconductors. To verify the ferroelectric properties of BTO NF, we conducted the piezoelectric force microscopy (PFM) measurement. (Fig. 4b and c). The PFM amplitude is nearly consistent with the AFM morphology, and a clear contrast can be observed in the phase image which implies different polarization directions (Fig. S5). The piezoelectric phase-voltage hysteresis loop exhibits an abrupt phase change from − 50° to 120° (nearly 180°) when the DC voltage was swept from − 10 to 10 V, confirming the polarization switching process of BTO NF [25,38]. Together with the butterfly shaped amplitude-voltage hysteresis loop, the excellent ferroelectric response of our microwave-synthesized BTO NF was confirmed.
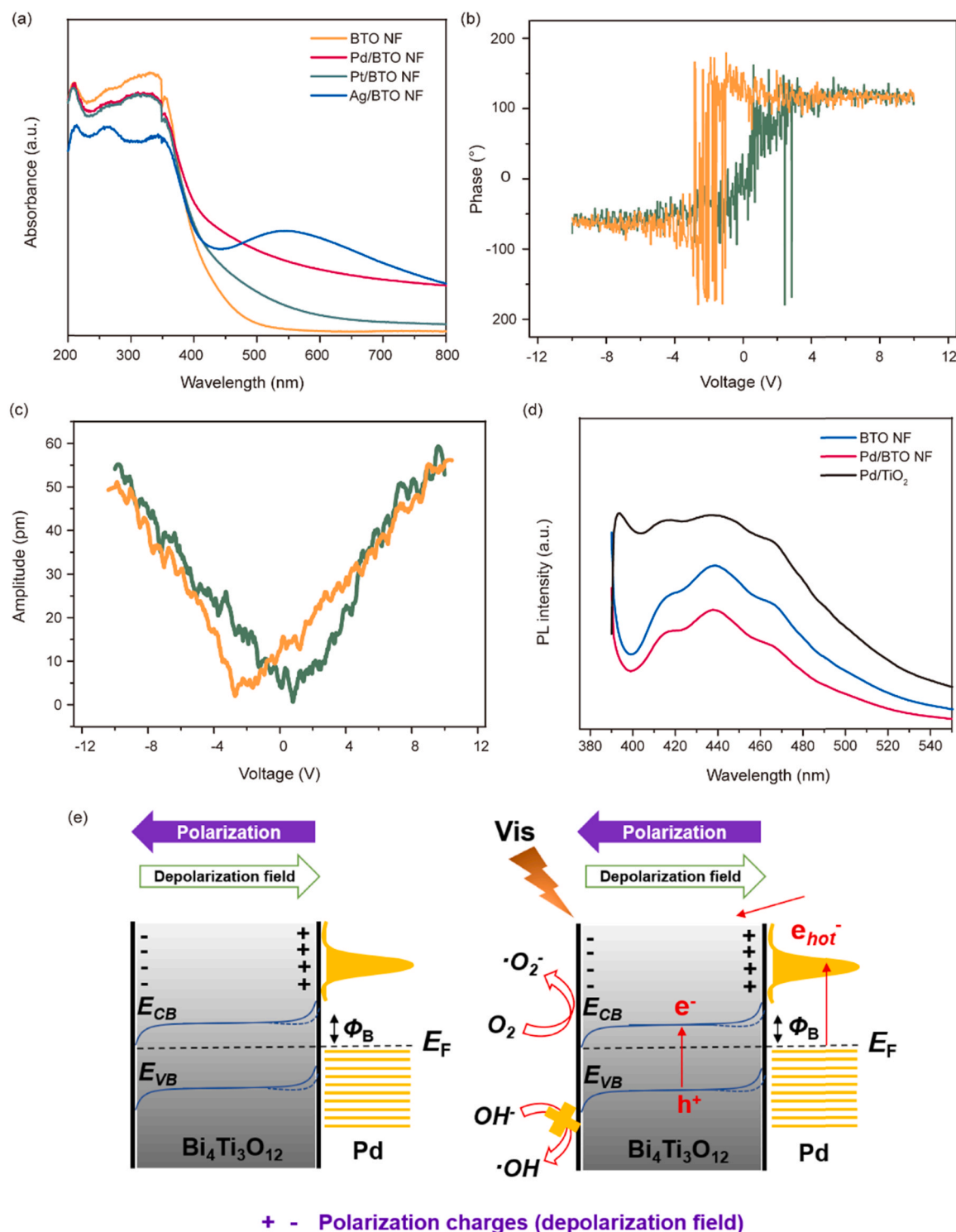
Fig. 4. Optical and charge separation properties. (a) Ultraviolet-visible diffuse reflectance spectra (extinction spectra) of various photocatalysts. (b) Piezoelectric force microscopy phase-voltage hysteresis loops of BTO NF. (c) Piezoelectric force microscopy amplitude-voltage butterfly loops of BTO NF. (d) Photoluminescence (PL) spectra of various photocatalysts. (e) Proposed mechanism for band alignment and the charge transfer process across Pd/BTO NF under visible light irradiation ($\lambda > 420$ nm).

In consequence, the ferroelectric character of BTO NF leads to low charge recombination rate as compared with TiO_2, which can explain the enhanced activity of Pd/BTO NF. The assumption is further supported by the photoluminescence (PL) spectra and transient photocurrent measurement (Fig. 4c and Fig. S6), which display that Pd/BTO NF possessed the lowest PL intensity and the highest photocurrent response comparing with BTO NF and Pd/TiO₂. The results confirmed superior

bulk charge separation ability of ferroelectric BTO NF, and together with the visible light response, the impressive NO photooxidation performance and activity enhancement of Pd/BTO NF was realized.

To explore how the charge injection process occurred between the Pd-BTO NF interface under visible light irradiation, we conducted a Mott-Schottky measurement to obtain the conduction band (CB) position of BTO NF (Fig. S7) [39]. The plot showed that BTO NF had a

relatively negative CB potential of − 0.9 V compared with Ag/AgCl, that is, − 1.1 V *vs.* NHE at 25 °C. The work function (*W*) of bulk Pd was 5.12 eV. According to the equation: $W = W_{bulk} + 1.08/d$, the work function of metal particles (W) is size dependent [21,40], and therefore, as particle size decreases, the Fermi level should be shifted upward. The *W* of Pd particles (average diameter: $d = 15$ nm) on the Pd/BTO NF was therefore determined to be 5.192 eV. The height of the Schottky barrier created at the Pd-BTO interface was calculated, with the equation $\varphi_B = W - \chi$, to be 1.792 eV ($\lambda = 692$ nm) [21]. That energy is smaller than the light irradiated on the Pd/BTO NF system ($\lambda \geq 420$ nm), which indicates that the charge injection from Pd to CB of BTO is possible.

On the basis of above discussions, we tentatively proposed a band alignment and charge transfer mechanism of NO photo-oxidation on Pd/BTO NF as follows (Fig. 4d). Before illumination, due to the different Fermi levels and the existence of depolarization electric field within ferroelectric BTO NF, charge carriers redistributed at the interface when Pd and BTO comes into contact, resulting in electron flow and decreased Schottky barrier (φ_B) across the interface. Upon visible light irradiation ($\lambda > 420$ nm), both BTO and Pd can be photo-excited, and the photo-excited hot electrons (e_{hot}^-) on Pd nanoparticles can transfer across the Schottky barrier to CB of BTO and reduce pre-adsorbed O_2. Meanwhile,

the photo-excited holes (h^+) on BTO can be driven apart by the depolarization field. However, the oxidation reaction of surface -OH groups with photo-excited h^+ cannot take place due to the VB position (1.65 V *vs.* NHE) is not oxidative enough to produce·OH. The ferroelectric polarization induced built-in electric field in BTO NF is vital for promoting charge carrier mobility and suppressing the recombination of photo-generated charge carriers.

3.3.2. Active species and selectivity

To confirm the above proposed mechanism, and explore the reason for high selectivity of Pd/BTO NF compared with Ag and Pt supported BTO NF, we investigated the molecular oxygen activation and the formation of reactive oxygen species (ROS). Firstly, the scavenging tests were performed with isopropanol, benzoquinone, potassium dichromate, and potassium iodide added to identify $\cdot O_2^-$, $\cdot OH$, e^- and h^+, respectively. As can be seen from Fig. 5a, benzoquinone significantly suppressed NO removal for Pd/BTO NF, suggesting·O_2^- to be the key photogenerated ROS. Employing 5,5-Dimethyl-1-Pyrroline-N-Oxide (DMPO) as the trapping reagent, the EPR spectra provided further direct evidence which confirmed ·O_2^- to be the predominant ROS. As observed from Fig. 5b, the sextet characteristic peak signal appeared
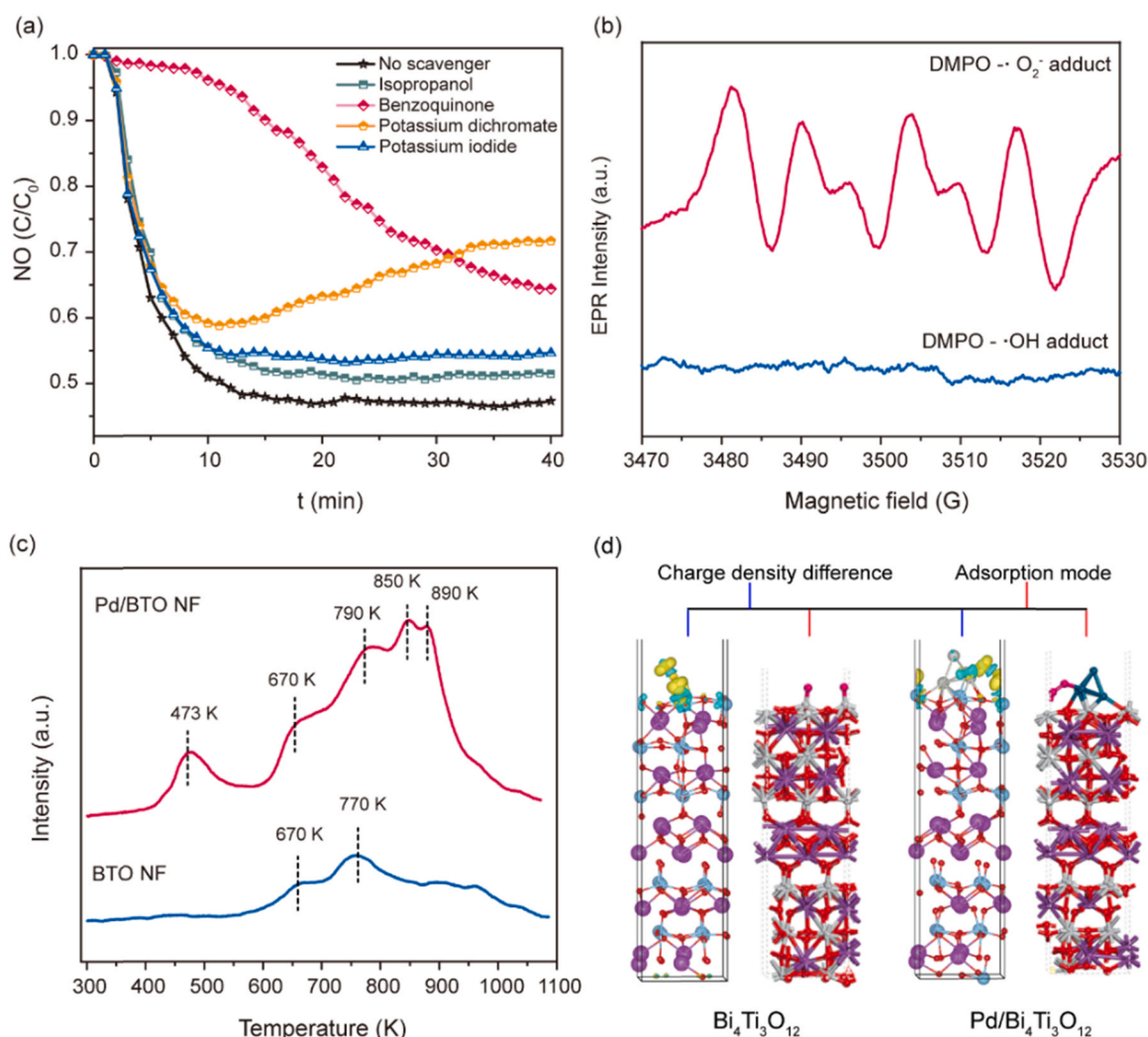

Fig. 5. O_2 activation studies. (a) Photocatalytic NO removal by Pd/BTO NF in the presence of selected scavengers. (b) Electronic paramagnetic resonance spectra of Pd/BTO NF suspended in water with visible light irradiation ($\lambda > 420$ nm) for 15 min (c) O_2 temperature-programmed desorption profiles of BTO NF and Pd/BTO NF. The samples were pretreated at 100 °C in He flow for 30 min, then cooled and purged in O_2 flow at 25 °C for 40 min, and the measurements were performed under He flow at a heating rate of 10 K min^{-1}. (d) Charge density difference of O_2 adsorbed BTO (100) and Pd$_4$/BTO (100) (charge accumulation in yellow and depletion in blue), and O_2 adsorption mode at the BTO (100) and Pd$_4$/BTO (100) surface, respectively.

corresponding to the DMPO-·O_2^- adduct, whereas the negligible signal for DMPO-·OH adduct was detected indicating its minor role contributing for NO removal under visible light. Indeed, some other studies have ascribed the observed sextet peaks to •OOH signals; [41,42] and this is because the superoxide anion is easily protonated to yield •OOH in acidic solution [43]. For comparisons, the photogenerated ROS of Ag/BTO NF, Pt/BTO NF and Pd/TiO$_2$ were also identified shown in Fig. S8. A 1:1:1 triplet signal appeared for Ag/BTO NF indicating the generation of $^1O_2$ [44]. Besides, the presence of typical signals (a^N = 7.2 G, $a^{\beta-2H}$ = 4.1 G) is attributed to 5,5-dimethyl-1-pyrrolidone-2-oxyl (DMPOX), which is derived from DMPO oxidation with H$_2$O$_2$. Comparing with Ag/BTO NF, weak signals for DMPO-·OOH and DMPO-·OH adducts were observed for Pt/BTO NF; and obvious signals for DMPO-·O_2^- adduct were detected for Pd/TiO$_2$. As a result, the photogenerated ROS are markedly different among these photocatalysts. The production of •O_2^- and •OOH promotes direct NO$_3^-$ formation,

while·OH facilitates stepwise NO oxidation *via* the NO$_{ad}$→HONO$_{ad}$→(NO$_2$)$_{ad}$→(HONO$_2$)$_{ad}$ route [11]. In this process, (NO$_2$)$_{ad}$ is easily desorbed from photocatalyst surface and enters into gas phase, thereby resulting in low selectivity. Based on these results and analysis, we believe that the single production of ·O_2^- is the primary cause for Pd/BTO NF possessing the excellent selectivity, while the production of ·OH and H$_2$O$_2$ which is easily break down into •OH radicals explain the poor selectivity of Ag/BTO NF and Pt/BTO NF.

To further investigate whether Pd nanoparticle deposition promoted O$_2$ adsorption, temperature-programmed oxygen desorption (O$_2$-TPD) experiments were conducted (Fig. 5c). Compared with the pristine BTO NF, Pd/BTO NF showed a desorption peak at 473 K, and intense desorption peaks at 670, 790, 850 and 890 K. The high temperature desorption peaks above 670 K were associated with lattice oxygen desorption, indicating that large amounts of lattice oxygen in BTO can be pulled out in the presence of Pd [45]. The peak at 473 K was probably
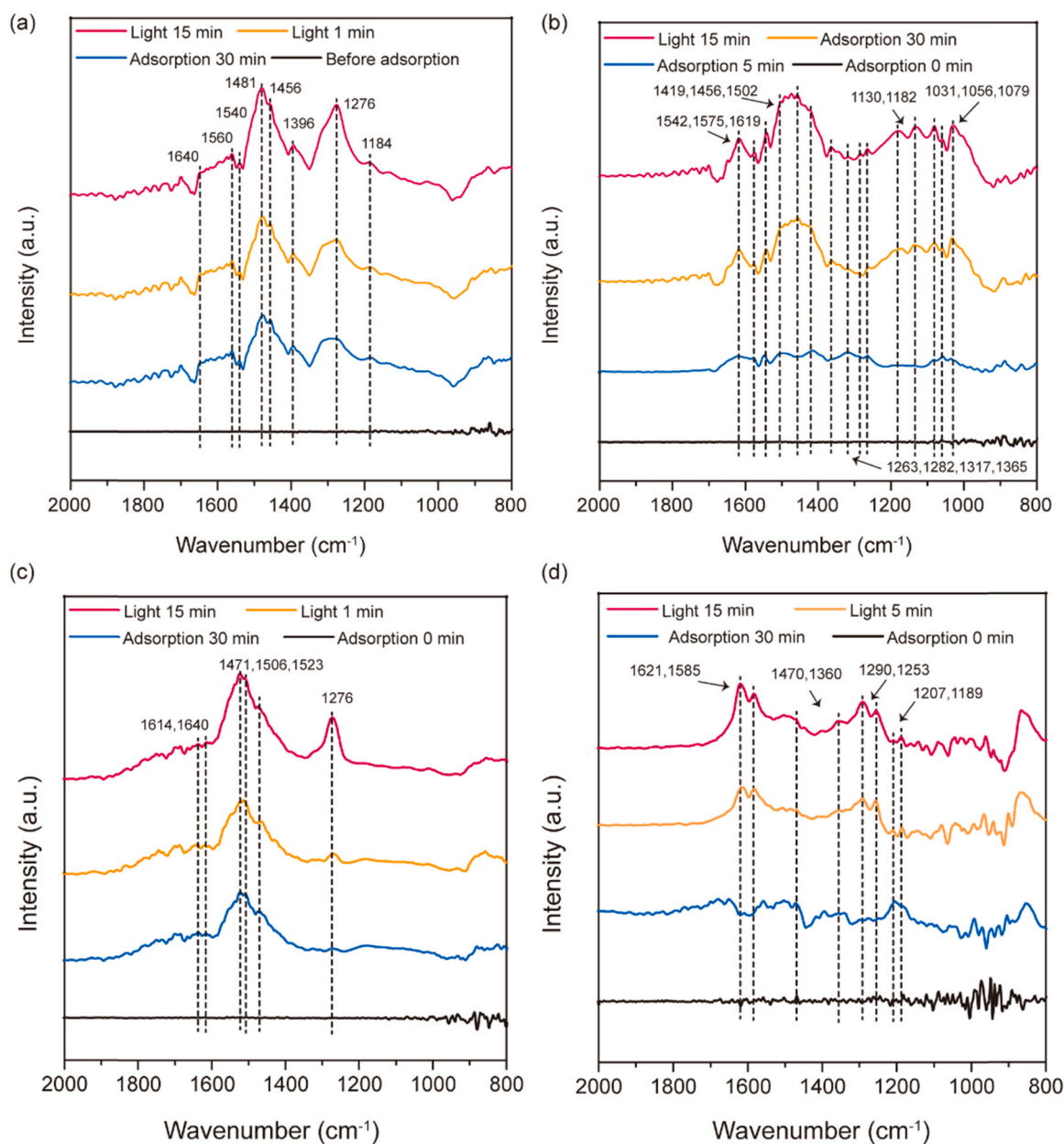
Fig. 6. *In situ* DRIFT spectra of NO and O$_2$ co-adsorbed onto the photocatalysts in the dark and under visible light irradiation for different time periods at 298 K. (a) Pd/BTO NF; (b) Ag/BTO NF; (c) Pt/BTO NF; (d) Pd/TiO$_2$. The catalysts were purged with He (flow rate = 50 mL min^{-1}) at 100 °C for 30 min. The NO and O$_2$ were introduced into the cell at 298 K and left for 30 min in the dark or under irradiation (λ > 420 nm).

assigned to surface active oxygen species, implying the efficient adsorption of O_2 at low temperatures [46]. DFT calculations were performed on BTO (100) plane and Pd_4/BTO (100) models, respectively, to investigate the activation of O-O bond. The charge density difference and adsorption mode of BTO and Pd_4/BTO surface with adsorbed O_2 models were calculated as shown in Fig. 5d. It can be observed that 2.06 e^- were accumulated on O_2 over the BTO surface, whereas 1.29 e^- were transferred to O_2 from Pd_4/BTO surface. This leads to the dissociation of O—O bond on BTO surface, whereas a bridge-type adsorption between the Pd/BTO interface with O—O bond length of 1.384 Å and adsorption energy of 2.88 eV. The result indicates that electrons were withdrawn from Pd and accumulated at the Pd/BTO interface, in accordance with the XPS results, confirming that the ferroelectric properties of BTO induces a strong metal-support interaction and different O_2 activation process.

We used *in situ* DRIFTS with NO as the probing molecule to obtain detailed information concerning reaction mechanism and selectivity in the presence of O_2. Fig. 6a shows time-resolved spectra of Pd/BTO NF in the dark and under visible light irradiation, respectively. After adsorption for 30 min, clear peaks were apparent at 1276 cm^{-1}, 1481 cm^{-1}, and trace peaks at 1184 cm^{-1}, 1396 cm^{-1}, 1456 cm^{-1}, 1540 cm^{-1}, 1560 cm^{-1} and 1640 cm^{-1} also appeared [47–50]. The weak peaks at 1184 cm^{-1} and 1396 cm^{-1} were assigned to nitrite and nitro species, whereas the other peaks are attributed to monodentate or bidentate nitrate (NO_3^-) species, which is evidence that strongly adsorbed species were formed. With light irradiation, the intensity of the bands assigned to monodentate nitrate (1276 cm^{-1}) and the symmetric stretching mode of bidentate nitrate (1456 cm^{-1}) gradually increased with time. In the meantime, other adsorption bands remained unchanged, and no new peaks associated with nitrite species were detected. These results showed that visible light promoted the photooxidation of NO over Pd/BTO NF with NO_3^- as the main product; and this is consistent with the high selectivity.

To follow up on the results showing the impact of supported metal nanoparticles on photocatalytic activity and selectivity, we investigated the interactions of NO + O_2 mixtures with different photocatalysts in the dark and under irradiation. The adsorption and photooxidation bands of NO on Ag/BTO NF are displayed in Fig. 6b. Different from Pd/BTO NF, adsorption peaks in the range of 1000–1200 cm^{-1} appeared after adsorption for 30 min. These bands are associated with bidentate or monodentate nitrite species. The peaks at 1419, 1456, and 1502 cm^{-1} increased significantly after adsorption from 5 min to 30 min, and that was accompanied by decreased intensity of the peak at 1317 cm^{-1}. This suggests that nitro species (1317 cm^{-1}) were likely to transform into nitrate species (1419, 1456, and 1502 cm^{-1}) after longer exposure times. With illumination the intensity of bands at 1282 cm^{-1} and those in the range of 1000–1200 cm^{-1} showed small enhancements, indicating the simultaneous generation of nitrate and nitrite species. For Pt/BTO NF exposed to NO in the dark and under illumination (Fig. 6c), the main differences observed were as follows: three obvious peaks at 1471, 1506 and 1523 cm^{-1} and a trace peak at 1276 cm^{-1} appeared after adsorption for 30 min in the dark, whereas those peaks were not evident for the other photocatalysts. These peaks were all assigned to NO_3^-, also indicating strongly adsorbed species were formed. With illumination, a significant increase in the intensity of the peak at 1276 cm^{-1} was observed, and this is a strong indication that nitrate species were the primary products at the Pt/BTO NF surfaces.

Fig. 6d shows that Pd/TiO_2 displayed no significant signals after exposure in NO + O_2 mixtures for 30 min, except for a small peak at 1207 cm^{-1}, which is possibly related to nitrite adsorbed on Pd^{2+} sites, and a trace band at 1360 cm^{-1} that is associated with adsorbed NO_2 on the anatase surface. Upon illumination, the obvious peaks at 1621, 1585, 1290 and 1253 cm^{-1} assigned to NO_3^- emerged and evolved with time; meanwhile, the intensity of bands at 1360 and 1207 cm^{-1} decreased [51]. This result indicates that supported Pd nanoparticles promote photooxidation of NO to NO_3^- and also explains the high

selectivity, both of which are in good agreement with previous studies [16].

We also conducted NO-TPD measurements to assess the effect of oxide support on NO adsorption and reaction for Pd/BTO NF and Pd/TiO_2, respectively (Fig. S9). The obvious desorption peak at ~ 609 K and trace desorption peaks at 427, 786, 856 and 973 K were observed for Pd/TiO_2. The peaks at 427 K and 609 K were assigned to NO desorption from TiO_2 and Pd sites, respectively. The high temperature peak at around 973 K is due to the decomposition of nitrates. In comparison, the low temperature desorption peaks at around 427 and 609 K disappeared, while high temperature peaks at 767, 834, and 884 K become significant for Pd/BTO NF. These results indicate that the addition of Pd nanoparticles to BTO NF surfaces increases the desorption of nitrate-related species, suggesting the high selectivity of Pd towards NO photooxidation; this is consistent with *in situ* DRIFT spectra. Therefore, through tuning the deposited metal types and supports, Pd/BTO NF was optimized to exhibit the best NO removal performance and superior selectivity to nitrates. The improved selectivity can be ascribed to excellent NO adsorption and the selective generation of •O_2^- radicals.

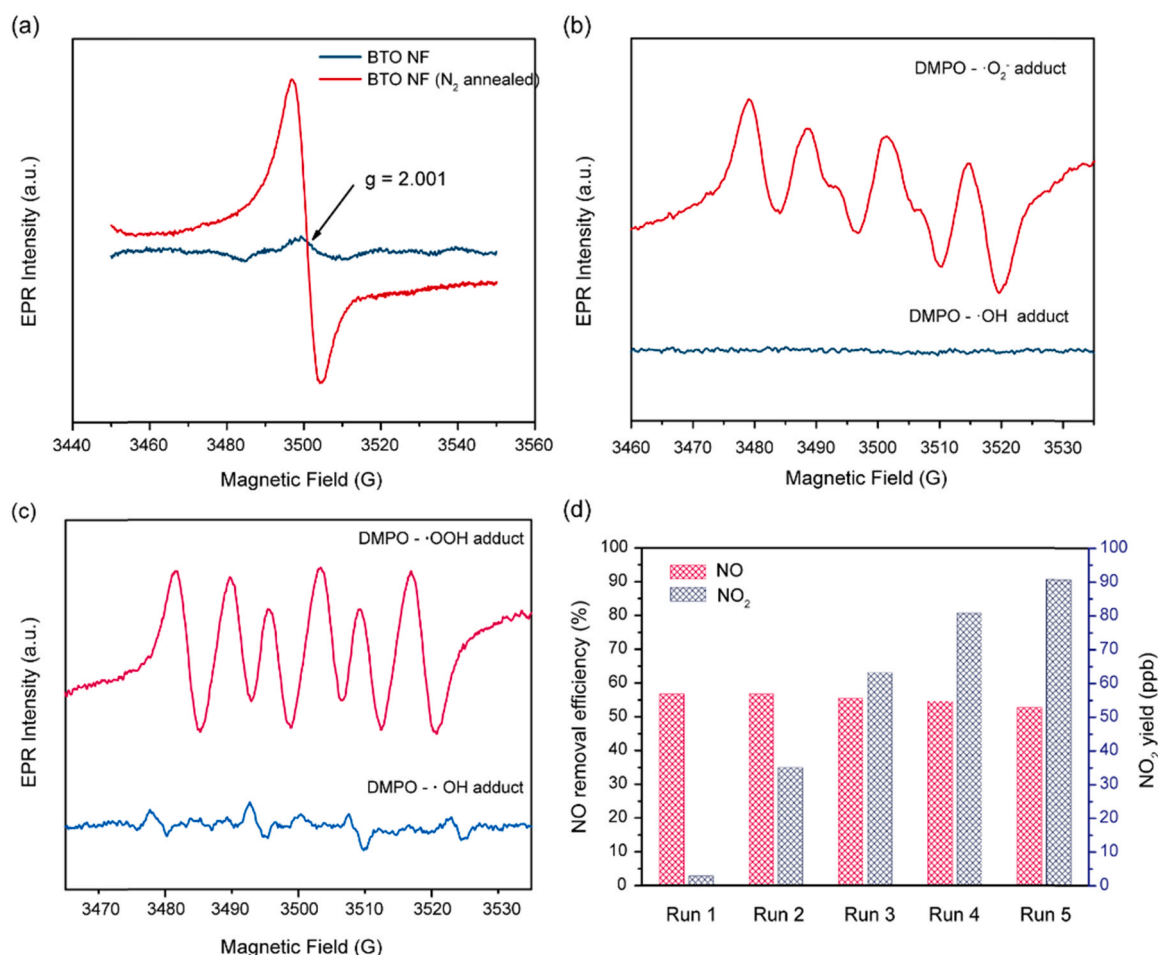### 3.3.3. Effect of interface oxygen vacancies

Atomic structures at the metal/oxide interface play a crucial role in mediating charge distribution and O_2 activation, thereby affecting heterogeneous catalytic activity and selectivity [20]. We created oxygen vacancies at the BTO NF surface by annealing in N_2 atmosphere at 673 K before photo-deposition of Pd nanoparticles. As shown in Fig. 7a, compared to the pristine BTO NF, a new EPR signal with *g*-factor at 2.001 appeared, suggesting the formation of oxygen vacancies [52]. Fig. 7b and c shows that different from BTO NF that only produced •O_2^- radicals, both •OOH and •OH radicals were generated in the presence of N_2 annealed Pd/BTO NF under light irradiation. As a result, the NO removal performance was slightly enhanced, but the NO_3^- selectivity decreased dramatically as the stability tests continue to proceed (Fig. 7d). This result further confirmed that •OH radicals are unfavorable for selectivity enhancement. Manipulating the metal/oxide interface structure seems to be vital for tuning ROS generation and NO photo-oxidation selectivity.

4. Conclusions

In conclusion, we have successfully prepared ferroelectric Pd/$Bi_4Ti_3O_{12}$ nanoflakes as effective visible-light-driven photocatalysts for NO photooxidation, and compared the performance with Ag and Pt supported BTO NF, as well as Pd/TiO_2. The Pd/BTO NF exhibited excellent NO removal with high selectivity due to a combination of various reasons. UV–vis analysis reveals that the BTO NF with bismuth rich surface extends light absorption into visible region, and the transition of *4d* electrons on Pd further promoted visible light harvest. The PFM and PL results reveal that unscreened depolarization field exists in BTO NF and leads to low charge recombination rate. Due to the low Schottky barrier, e_{hot} on Pd nanoparticles could be injected into conduction band of BTO, thereby enhancing the photocatalytic activity. EPR results reveal •O_2^- to be the primary ROS for Pd/BTO NF, whereas Ag/BTO NF and Pt/BTO possess other radicals except •O_2^-. The enhanced O_2 adsorption and activation derived from TPD analysis and DFT calculations also ensure the superior performance of Pd/BTO NF. The present work highlights the potential of microwave synthesis for inorganic perovskite nanomaterials, and the promising application of ferroelectric photocatalysts for pollutant remediation and beyond.

Supporting information

The scheme of synthesis procedure; SEM and TEM images of $Bi_4Ti_3O_{12}$ nanoflakes; High resolution X-ray photoelectron spectra of Bi *4f* and Ti *2p* orbitals for $Bi_4Ti_3O_{12}$; High resolution XPS results of Ag *3d* and Pt *4f* orbitals for Ag/$Bi_4Ti_3O_{12}$ and Pt/$Bi_4Ti_3O_{12}$, respectively;

Fig. 7. Effect of interface oxygen vacancies. (a) X-band electronic paramagnetic resonance (EPR) spectra of pristine BTO NF and N_2 annealed BTO NF at 90 K. (b) EPR spectra of radical adduct by DMPO over BTO NF suspension with the visible light irradiation ($\lambda > 420$ nm). (c) EPR spectra of radical adduct by DMPO over Pd/BTO (N_2) NF suspension with the visible light irradiation ($\lambda > 420$ nm). (d) Stability performance of photocatalytic NO oxidation over Pd/BTO NF with N_2 annealing in 5 runs at 298 K. Reaction conditions: 400 ppb NO balanced with zero air at flow rate of 1 L min^{-1}, 300 W Xe lamp equipped with UV cut-off filter ($\lambda > 420$ nm).

Photocatalytic performances of Pd/$Bi_4Ti_3O_{12}$ with varying Pd contents and annealing; UV–vis spectra of Pd/$Bi_4Ti_3O_{12}$ with varying Pd contents; Ferroelectric properties of BTO NF; Transient photocurrent response of BTO NF; Mott-Schottky plot of BTO NF; EPR spectra of photocatalyst suspension in water under visible light illumination; NO temperature programmed desorption (TPD) profiles of Pd/TiO_2 and Pd/BTO NF.

CRediT authorship contribution statement

Qian Zhang: Conceptualization, Investigation, Methodology, Formal analysis, Writing – original draft, Writing – review & editing, Funding acquisition. **Yuanyu Shi:** Investigation, Methodology, Formal analysis. **Xianjin Shi:** Investigation. Methodology. **Tingting Huang:** Investigation, Methodology. **Shuncheng Lee:** Formal analysis, Writing – review & editing. **Yu Huang:** Conceptualization, Supervision, Resources, Writing – review & editing. **Jun-ji Cao:** Supervision, Writing – review & editing, Funding acquisition.

Declaration of Competing Interest

The authors declare that they have no known competing financial interests or personal relationships that could have appeared to influence the work reported in this paper.

Appendix A. Supporting information

Supplementary data associated with this article can be found in the online version at doi:10.1016/j.apcatb.2021.120876.

References

[1] Q. Zhang, Y.X. Zheng, D. Tong, M. Shao, S.X. Wang, Y.H. Zhang, X.D. Xu, J. N. Wang, H. He, W.Q. Liu, Y.H. Ding, Y. Lei, J.H. Li, Z.F. Wang, X.Y. Zhang, Y. S. Wang, J. Cheng, Y. Liu, Q.R. Shi, L. Yan, G.N. Geng, C.P. Hong, M. Li, F. Liu, B. Zheng, J.J. Cao, A.J. Ding, J. Gao, Q.Y. Fu, J.T. Huo, B.X. Liu, Z.R. Liu, F. M. Yang, K.B. He, J.M. Hao, Drivers of improved PM$_{2.5}$ air quality in China from 2013 to 2017, Proc. Natl. Acad. Sci. USA 116 (2019) 24463–24469, https://doi.org/10.1073/pnas.1907956116.

[2] G.Q. Tang, Y.S. Liu, J.Q. Zhang, B.X. Liu, Q.H. Li, J. Sun, Y.H. Wang, Y.J. Xuan, Y. T. Li, J.X. Pan, X. Li, Y.S. Wang, Bypassing the NO$_x$ titration trap in ozone pollution control in Beijing, Atmos. Res. 249 (2021), 105333, https://doi.org/10.1016/j.atmosres.2020.105333.

[3] A.J. Cohen, M. Brauer, R. Burnett, H.R. Anderson, J. Frostad, K. Estep, K. Balakrishnan, B. Brunekreef, L. Dandona, R. Dandona, V. Feigin, G. Freedman,

B. Hubbell, A. Jobling, H.D. Kan, L. Knibbs, Y. Liu, R. Martin, L. Morawska, C. A. Pope III, H. Shin, K. Straif, G. Shaddick, M. Thomas, R.V. Dingenen, A. V. Donkelaar, T. Vos, C.J.L. Murray, M.H. Forouzanfar, Estimates and 25-year trends of the global burden of disease attributable to ambient air pollution: an analysis of data from the Global Burden of Diseases Study 2015, Lancet 389 (2017) 1907–1918, https://doi.org/10.1016/S0140-6736(17)30505-6.

[4] L. Kang, L.P. Han, P.L. Wang, C. Feng, J.P. Zhang, T.T. Yan, J. Deng, L.Y. Shi, D. S. Zhang, SO_2-tolerant NO_x reduction by marvelously suppressing SO_2 adsorption over $Fe_\delta Ce_{1-\delta}VO_4$ catalysts, Environ. Sci. Technol. 54 (2020) 14066–14075, https://doi.org/10.1021/acs.est.0c05038.

[5] X.G. Li, C. Chen, C. Liu, H. Xian, L. Guo, J.L. Lv, Z. Jiang, P. Vernoux, Pd-doped perovskite: an effective catalyst for removal of NO_x from lean-burn exhausts with high sulfur resistance, ACS Catal. 3 (2013) 1071–1075, https://doi.org/10.1021/cs400136t.

[6] J.N. Li, X. Han, X.R. Zhang, A.M. Sheveleva, Y.Q. Cheng, F. Tuna, E.J.L. McInnes, L. J.M. McPherson, S.J. Teat, L.L. Daemen, A.J. Ramirez-Cuesta, M. Schröder, S. H. Yang, Capture of nitrogen dioxide and conversion to nitric acid in a porous metal-organic framework, Nat. Chem. 11 (2019) 1085–1090, https://doi.org/10.1038/s41557-019-0356-0.

[7] J.Z. Bloh, A. Folli, D.E. Macphee, Photocatalytic NO_x abatement: why the selectivity matters, RSC Adv. 4 (2014) 45726–45734, https://doi.org/10.1039/C4RA07916G.

[8] J. Patzsch, J.N. Spencer, A. Folli, J.Z. Bloh, Grafted iron(III) ions significantly enhance NO_2 oxidation rate and selectivity of TiO_2 for photocatalytic NO_x abatement, RSC Adv. 8 (2018) 27674–27685, https://doi.org/10.1039/C8RA05017A.

[9] G.F. Guo, Y. Hu, S.M. Jiang, C.H. Wei, Photocatalytic oxidation of NO_x over TiO_2/HZSM-5 catalysts in the presence of water vapor: effect of hydrophobicity of zeolites, J. Hazard. Mater. 223–224 (2012) 39–45, https://doi.org/10.1016/j.jhazmat.2012.04.043.

[10] G.H. Dong, L.P. Yang, F. Wang, L. Zang, C.Y. Wang, Removal of nitric oxide through visible light photocatalysis by g-C_3N_4 modified with perylene imides, ACS Catal. 6 (2016) 6511–6519, https://doi.org/10.1021/acscatal.6b01657.

[11] A. Folli, J.Z. Bloh, K. Armstrong, E. Richards, D.M. Murphy, L. Lu, C.J. Kiely, D. J. Morgan, R.I. Smith, A.C. Mclaughlin, D.E. Macphee, Improving the selectivity of photocatalytic NO_x abatement through improved O_2 reduction pathways using $Ti_{0.909}W_{0.091}O_2N_x$ semiconductor nanoparticles: from characterization to photocatalytic performance, ACS Catal. 8 (2018) 6927–6938, https://doi.org/10.1021/acscatal.8b00521.

[12] H. Shang, M.Q. Li, H. Li, S. Huang, C.L. Mao, Z.H. Ai, L.Z. Zhang, Oxygen vacancies promoted selective photocatalytic removal of NO with blue TiO_2 *via* simultaneous molecular oxygen activation and photogenerated holes annihilation, Environ. Sci. Technol. 53 (2019) 6444–6453, https://doi.org/10.1021/acs.est.8b07322.

[13] H. Li, H. Shang, X.M. Cao, Z.P. Yang, Z.H. Ai, L.Z. Zhang, Oxygen vacancies mediated complete visible light NO oxidation *via* side-on bridging superoxide radicals, Environ. Sci. Technol. 52 (2018) 8659–8665, https://doi.org/10.1021/acs.est.8b01849.

[14] M.M. Montemore, M.A.V. Spronsen, R.J. Madix, C.M. Friend, O_2 activation by metal surfaces: implications for bonding and reactivity on heterogeneous catalysts, Chem. Rev. 118 (2018) 2816–2862, https://doi.org/10.1021/acs.chemrev.7b00217.

[15] T. Pradeep, Anshup, Noble metal nanoparticles for water purification: a critical review, Thin Solid Films 517 (2009) 6441–6478, https://doi.org/10.1016/j.tsf.2009.03.195.

[16] K. Fujiwara, U. Muller, S.E. Pratsinis, Pd subnano-clusters on TiO_2 for solar-light removal of NO, ACS Catal. 6 (2016) 1887–1893, https://doi.org/10.1021/acscatal.5b02685.

[17] K. Fujiwara, S.E. Pratsinis, Single Pd atoms on TiO_2 dominate photocatalytic NO_x removal, Appl. Catal. B: Environ. 226 (2018) 127–134, https://doi.org/10.1016/j.apcatb.2017.12.042.

[18] H. Hao, B.F. Jin, W. Liu, X.D. Wu, F.F. Yin, S. Liu, Robust $Pt@TiO_x/TiO_2$ catalysts for hydrocarbon combustion: effects of Pt-TiO_x interaction and sulfates, ACS Catal. 10 (2020) 13543–13548, https://doi.org/10.1021/acscatal.0c03984.

[19] N. Siemer, A. Luken, M. Zalibera, J. Frenzel, D. Muñoz-Santiburcio, A. Savitsky, W. Lubitz, M. Muhler, D. Marx, J. Strunk, Atomic-scale explanation of O_2 activation at the Au-TiO_2 interface, J. Am. Chem. Soc. 140 (2018) 18082–18092, https://doi.org/10.1021/jacs.8b10929.

[20] J.W. Huang, S. He, J.L. Goodsell, J.R. Mulcahy, W. Guo, A. Angerhofer, W.D. Wei, Manipulating atomic structures at the Au/TiO_2 interface for O_2 activation, J. Am. Chem. Soc. 142 (2020) 6456–6460, https://doi.org/10.1021/jacs.9b13453.

[21] H. Sakamoto, T. Ohara, N. Yasumoto, Y. Shiraishi, S. Ichikawa, S. Tanaka, T. Hirai, Hot-electron-induced highly efficient O_2 activation by Pt nanoparticles supported on Ta_2O_5 driven by visible light, J. Am. Chem. Soc. 137 (2015) 9324–9332, https://doi.org/10.1021/jacs.5b04062.

[22] L. Brugnoli, A. Pedone, M.C. Menziani, C. Adamo, F. Labat, O_2 activation over Ag-decorated $CeO_2(111)$ and $TiO_2(110)$ surfaces: a theoretical comparative investigation, J. Phys. Chem. C 124 (2020) 25917–25930, https://doi.org/10.1021/acs.jpcc.0c09080.

[23] F. Wang, J.B. Wang, X.L. Zhong, B. Li, J. Liu, D. Wu, D. Mo, D.Y. Guo, S.G. Yuan, K. D. Zhang, Y.C. Zhou, Shape-controlled hydrothermal synthesis of ferroelectric $Bi_4Ti_3O_{12}$ nanostructures, CrystEngComm 15 (2013) 1397–1403, https://doi.org/10.1039/C2CE26330K.

[24] Y. Liu, S. Ye, H.C. Xie, J. Zhu, Q. Shi, N. Ta, R.T. Chen, Y.Y. Gao, H.Y. An, W. Nie, H.W. Jing, F.T. Fan, C. Li, Internal-field-enhanced charge separation in a single-domain ferroelectric $PbTiO_3$ photocatalyst, Adv. Mater. 32 (2020), 1906513, https://doi.org/10.1002/adma.201906513.

[25] H.J. Yu, F. Chen, X.W. Li, H.W. Huang, Q.Y. Zhang, S.Q. Su, K.Y. Wang, E.Y. Mao, Bastian Mei, Guido Mul, T.Y. Ma, Y.H. Zhang, Synergy of ferroelectric polarization and oxygen vacancy to promote CO_2 photoreduction, Nat. Commun. 12 (2021) 4594–4603, https://doi.org/10.1038/s41467-021-24882-3.

[26] B.Y. Zhang, G.X. Zhang, Interpretation of the surface charge decay kinetics on insulators with different neutralization mechanisms, J. Appl. Phys. 121 (2017) 105105–105124, https://doi.org/10.1063/1.4978001.

[27] M.B. Gawande, S.N. Shelke, R. Zboril, R.S. Varma, Microwave-assisted chemistry: synthetic applications for rapid assembly of nanomaterials and organics, Acc. Chem. Res. 47 (2014) 1338–1348, https://doi.org/10.1021/ar400309b.

[28] G. Kresse, J. Furthmüller, Efficiency of ab-initio total energy calculations for metals and semiconductors using a plane-wave basis set, Com. Mater. Sci. 6 (1996) 15–50, https://doi.org/10.1016/0927-0256(96)00008-0.

[29] J.P. Perdew, J.A. Chevary, S.H. Vosko, K.A. Jackson, M.R. Pederson, D.J. Singh, C. Fiolhais, Atoms, molecules, solids, and surfaces: applications of the generalized gradient approximation for exchange and correlation, Phys. Rev. B: Condens. Matter 46 (1992) 6671–6687, https://doi.org/10.1103/physrevb.46.6671.

[30] H.J. Monkhorst, J.D. Pack, Special points for Brillouin zone integrations, Phys. Rev. B: Condens. Matter 13 (1976) 5188–5192, https://doi.org/10.1103/PhysRevB.13.5188.

[31] Y.B. Liu, G.Q. Zhu, J.Z. Gao, M. Hojamberdiev, R.L. Zhu, X.M. Wei, Q.M. Guo, P. Liu, Enhanced photocatalytic activity of $Bi_4Ti_3O_{12}$ nanosheets by Fe^{3+}-doping and the addition of Au nanoparticles: photodegradation of Phenol and bisphenol A, Appl. Catal. B: Environ. 200 (2017) 72–82, https://doi.org/10.1016/j.apcatb.2016.06.069.

[32] Q. Pan, H.C. Hu, Y.T. Zou, M. Chen, L.Z. Wu, D. Yang, X.L. Yuan, J. Fan, B.Q. Sun, Q. Zhang, Microwave-assisted synthesis of high-quality "all-inorganic" $CsPbX_3$ (X = Cl, Br, I) perovskite nanocrystals and their application in light emitting diodes, J. Mater. Chem. C 5 (2017) 10947–10954, https://doi.org/10.1039/C7TC03774K.

[33] S.Y. Chen, S.D. Li, R.Y. You, Z.Y. Guo, F. Wang, G.X. Li, W.T. Yuan, B.E. Zhu, Y. Gao, Z. Zhang, H.S. Yang, Y. Wang, Elucidation of active sites for CH_4 catalytic oxidation over Pd/CeO_2 *via* tailoring metal-support interactions, ACS Catal. 11 (2021) 5666–5677, https://doi.org/10.1021/acscatal.1c00839.

[34] Y.L. Zhang, J.Y. Zhang, B.S. Zhang, R. Si, B. Han, F. Hong, Y.M. Niu, L. Sun, L. Li, B. T. Qiao, K.J. Sun, J.H. Huang, M. Haruta, Boosting the catalysis of gold by O_2 activation at Au-SiO_2 interface, Nat. Commun. 11 (2020) 558, https://doi.org/10.1038/s41467-019-14241-8.

[35] Q. Zhang, Y. Huang, L.F. Xu, J.J. Cao, W.K. Ho, S.C. Lee, Visible-Light-Active plasmonic Ag-$SrTiO_3$ nanocomposites for the degradation of NO in air with high selectivity, ACS Appl. Mater. Interfaces 8 (2016) 4165–4174, https://doi.org/10.1021/acsami.5b11887.

[36] W.K. Wang, J.J. Chen, W.W. Li, D.N. Pei, X. Zhang, H.Q. Yu, Synthesis of Pt-loaded self-interspersed anatase TiO_2 with a large fraction of (001) facets for efficient photocatalytic nitrobenzene degradation, ACS Appl. Mater. Interfaces 7 (2015) 20349–20359, https://doi.org/10.1021/acsami.5b06161.

[37] D.F. Hou, X.L. Hu, P. Hu, W. Zhang, M.F. Zhang, Y.H. Huang, $Bi_4Ti_3O_{12}$ nanofibers/BiOI nanosheets p-n junction: facile synthesis and enhanced visible-light photocatalytic activity, Nanoscale 5 (2013) 9764–9772, https://doi.org/10.1039/C3NR02458J.

[38] D.F. Yu, Z.H. Liu, J.M. Zhang, S. Li, Z.C. Zhao, L.F. Zhu, W.S. Liu, Y.H. Ling, H. Liu, Z.T. Zhang, Enhanced catalytic performance by multi-field coupling in $KNbO_3$ nanostructures: piezo-photocatalytic and ferro-photoelectrochemical effects, Nano Energy 58 (2019) 695–705, https://doi.org/10.1016/j.nanoen.2019.01.095.

[39] S. Zhu, X.F. Chen, Z.C. Li, X.Y. Ye, Y. Liu, Y. Chen, L. Yang, M. Chen, D.Q. Zhang, G. S. Li, H.X. Li, Cooperation between inside and outside of TiO_2: lattice Cu^+ accelerates carrier migration to the surface of metal copper for photocatalytic CO_2 reduction, Appl. Catal. B: Environ. 264 (2020) 118515–118524, https://doi.org/10.1016/j.apcatb.2019.118515.

[40] K. Kim, J. Park, H. Kim, G.Y. Jung, M.G. Kim, Solid-Phase photocatalysts: physical vapor deposition of Au nanoislands on porous TiO_2 films for millimolar H_2O_2 production within a few minutes, ACS Catal. 9 (2019) 9206–9211, https://doi.org/10.1021/acscatal.9b02269.

[41] H. Song, X.G. Meng, S.Y. Wang, W. Zhou, S. Song, T. Kako, J.H. Ye, Selective photo-oxidation of methane to methanol with oxygen over dual-cocatalyst-modified titanium dioxide, ACS Catal. 10 (2020) 14318–14326, https://doi.org/10.1021/acscatal.0c04329.

[42] F.A. Villamena, J.L. Zweier, Detection of reactive oxygen and nitrogen species by EPR spin trapping, Antioxid. Redox Signal. 6 (2004) 619–629, https://doi.org/10.1089/152308604773934387.

[43] Z.H. Wang, W.H. Ma, C.C. Chen, H.W. Ji, J.C. Zhao, Probing paramagnetic species in titania-based heterogeneous photocatalysis by electron spin resonance (ESR) spectroscopy-a mini review, Chem. Eng. J. 170 (2011) 353–362, https://doi.org/10.1016/j.cej.2010.12.002.

[44] H. Wang, S.C. Chen, D.Y. Yong, X.D. Zhang, S. Li, W. Shao, X.S. Sun, B.C. Pan, Y. Xie, Giant electron-hole interactions in confined layered structures for molecular oxygen activation, J. Am. Chem. Soc. 139 (2017) 4737–4742, https://doi.org/10.1021/jacs.6b12273.

[45] M. Haneda, T. Mizushima, N. Kakuta, Synergistic effect between Pd and nonstoichiometric cerium oxide for oxygen activation in methane oxidation, J. Phys. Chem. B 102 (1998) 6579–6587, https://doi.org/10.1021/jp9819285.

[46] T. Fujita, T. Ishida, K. Shibamoto, T. Honma, H. Ohashi, T. Murayama, M. Haruta, CO oxidation over Au/ZnO: unprecedented change of the reaction mechanism at low temperature caused by a different O_2 activation process, ACS Catal. 9 (2019) 8364–8372, https://doi.org/10.1021/acscatal.9b02128.

[47] J.C.S. Wu, Y.T. Cheng, *In situ* FTIR study of photocatalytic NO reaction on photocatalysts under UV irradiation, J. Catal. 237 (2006) 393–404, https://doi.org/10.1016/j.jcat.2005.11.023.

[48] X. Feng, W.D. Zhang, Y.J. Sun, H.W. Huang, F. Dong, Fe(III) clusters-grafted (BiO)$_2$CO$_3$ superstructures: *in situ* DRIFTS investigation on IFCT-enhanced visible light photocatalytic NO oxidation, Environ. Sci.: Nano 4 (2017) 604–612, https://doi.org/10.1039/C6EN00637J.

[49] Y. Liu, S. Yu, Z.Y. Zhao, F. Dong, X.A. Dong, Y. Zhou, N-doped Bi$_2$O$_2$CO$_3$/graphene quantum dot composite photocatalyst: enhanced visible-light photocatalytic NO oxidation and *in situ* DRIFTS studies, J. Phys. Chem. C 121 (2017) 12168–12177, https://doi.org/10.1021/acs.jpcc.7b02285.

[50] Q. Zhang, Y. Huang, S.Q. Peng, T.T. Huang, J.J. Cao, W.K. Ho, S.C. Lee, Synthesis of SrFe$_x$Ti$_{1-x}$O$_{3-\delta}$ nanocubes with tunable oxygen vacancies for selective and efficient photocatalytic NO oxidation, Appl. Catal. B: Environ. 239 (2018) 1–9, https://doi.org/10.1016/j.apcatb.2018.07.076.

[51] Q. Wu, C.C. Yang, R.V.D. Krol, A dopant-mediated recombination mechanism in Fe-doped TiO$_2$ nanoparticles for the photocatalytic decomposition of nitric oxide, Catal. Today 225 (2014) 96–101, https://doi.org/10.1016/j.cattod.2013.09.026.

[52] A. Naldoni, M. Altomare, G. Zoppellaro, N. Liu, Š. Kment, R. Zbořil, P. Schmuki, Photocatalysis with reduced TiO$_2$: from black TiO$_2$ to cocatalyst-free hydrogen production, ACS Catal. 9 (2019) 345–364, https://doi.org/10.1021/acscatal.8b04068.